



## In-Situ Atomic-Scale Observation of Inhomogeneous Oxide Reduction

Journal:	<i>ChemComm</i>
Manuscript ID	CC-COM-05-2018-003822.R1
Article Type:	Communication

SCHOLARONE™  
Manuscripts



ChemComm

COMMUNICATION

## In-Situ Atomic-Scale Observation of Inhomogeneous Oxide Reduction

Received 00th January 20xx,  
Accepted 00th January 20xx

Xiaobo Chen,<sup>a</sup> Dongxiang Wu,<sup>a</sup> Lianfeng Zou,<sup>a</sup> Qiyue Yin,<sup>a</sup> Hanlei Zhang,<sup>a</sup> Dmitri N. Zakharov,<sup>b</sup> Eric A. Stach,<sup>c</sup> and Guangwen Zhou<sup>a\*</sup>

DOI: 10.1039/x0xx00000x

www.rsc.org/chemcomm

**We report in-situ atomic-scale transmission electron microscopy observations of the surface dynamics during the Cu<sub>2</sub>O reduction. We show inhomogeneous oxide reduction caused by the preferential adsorption of hydrogen at step edges that induces oxygen loss and destabilizes Cu atoms within the step edge, thereby resulting in the retraction motion of atomic steps at the oxide surface.**

Reduction is widely used to modify the stoichiometry,<sup>1</sup> phase,<sup>2</sup> coordination,<sup>3</sup> bonding, defects<sup>4,5</sup> and atomic termination of metal oxides,<sup>6</sup> thereby tuning their functional properties for a wide variety of applications ranging from catalysis to electronic devices.<sup>7,8</sup> Oxide reduction is induced by the loss of lattice oxygen and the oxide reducibility thus depends on the ability of the oxide to release oxygen.<sup>2-9</sup> Oxide reduction typically involves multiple hierarchical length scales and proceeds generally via the adsorption of a reducing agent (e.g., H<sub>2</sub>, CO), its reaction with the lattice oxygen to form gas molecules (e.g., H<sub>2</sub>O, CO<sub>2</sub>) that desorb from the surface and then the oxygen-loss induced phase and microstructure evolution.<sup>10,11</sup> For reactions occurring on such multiple length and time scales, factors influencing the reaction mechanisms are many, and are both macroscopic (geometry, support, etc.) and microscopic (defects, interfaces, atomic transport, etc.).<sup>12,13</sup> Averaging tools have been widely used to study oxide reduction on the global scale, including temperature-programmed reduction (TPR) to monitor oxide reduction induced oxygen loss and X-ray diffraction to understand oxide reduction induced structural and phase evolution.<sup>14,15</sup> However, significant challenges exist in controlling the oxide reduction processes, particularly at the atomic scale.<sup>16,17</sup> Several reasons for this include the long-standing challenges in performing microscopic measurements on the oxide surfaces. This is because many surface-sensitive techniques are based on charged particles (electrons, ions) and cannot be applied to oxides which are usually insulating (or wide-gap) materials.<sup>18,19</sup>

Transmission electron microscopy (TEM) has evolved dramatically in recent years to allow temperature- and pressure-resolved imaging/diffraction of gas-surface reactions at the atomic scale.<sup>20,21</sup> This is accomplished by differentially pumped environmental TEM and the incorporation of aberration correction techniques. Environmental TEM thus provides an elegant solution to directly observe, at the atomic-scale, the dynamics of oxide reduction at elevated pressure and temperature.<sup>18-22</sup> With the use of environmental TEM techniques, we have shown that the reduction of Cu<sub>2</sub>O nanoislands occurs via step flow along the buried Cu<sub>2</sub>O/Cu interface and accumulation of oxygen vacancies near the Cu<sub>2</sub>O/Cu interface region results in the abrupt collapse of the Cu<sub>2</sub>O lattice that drives the rotation of a Cu<sub>2</sub>O island.<sup>17</sup> In this work, we deal with the reduction of a thick Cu<sub>2</sub>O layer that resembles a bulk sample. Using environmental TEM, we find that the oxide reduction for the bulk-like Cu<sub>2</sub>O layer takes place at the oxide surface and the Cu<sub>2</sub>O→Cu transformation is controlled by surface defects (e.g., atomic steps) at the oxide surface, which differs from the Cu<sub>2</sub>O/Cu interface controlled oxide reduction and demonstrates the complexity of the reaction mechanism that can depend on sample size, geometry, and atomic defects.

The oxide reduction experiments were performed in a dedicated environmental TEM (FEI Titan 80-300) equipped with an objective-lens aberration corrector. Cu single-crystal thin films with ~ 500 Å were grown on NaCl substrates by e-beam evaporation and the Cu films were then removed from the substrate by floatation in deionized water, washed, and mounted on a TEM specimen holder. Our in-situ TEM experiment involved a two-step process. First, the Cu film was annealed at ~ 600 °C in H<sub>2</sub> gas flow (pH<sub>2</sub> = 10<sup>-3</sup> Torr), which reduced the native Cu oxides to Cu and generated tears and holes with faceted edges. The annealed Cu film was then oxidized at 350 °C by introducing oxygen gas at pO<sub>2</sub> = 5×10<sup>-3</sup> Torr to form free-standing Cu<sub>2</sub>O films that grew into the empty space of the hole area (see Supplementary Note 1). The Cu<sub>2</sub>O film was then reduced at 350 °C by flowing H<sub>2</sub> gas and in-situ TEM observations of the Cu<sub>2</sub>O reduction were made in both planar and cross-sectional views. Cu<sub>2</sub>O is a highly reducible oxide and the reduction rate can be fast at the elevated temperature when the hydrogen gas pressure is sufficiently high. In our experiment, a low hydrogen pressure (1.2×10<sup>-2</sup> Torr) was used, for which the reaction rate is relatively slow, thereby allowing for monitoring the atomic process of the oxide reduction.

<sup>a</sup> Program of Materials Science and Engineering & Department of Mechanical Engineering, State University of New York at Binghamton, NY 13902, USA. Email: gzhou@binghamton.edu

<sup>b</sup> Center for Functional Nanomaterials, Brookhaven National Laboratory, Upton, NY 11973, USA

<sup>c</sup> Department of Materials Science and Engineering, University of Pennsylvania, Philadelphia, PA 19104, USA

† Electric supplementary information (ESI) available: Specimen preparation and DFT calculation details. See DOI: 10.1039/x0xx00000x

To ensure that we observed intrinsic behaviour of the surface phenomena, an imaging protocol based on low-dose microscopy techniques was adopted to minimize the effects of electron beam irradiation, including performing focusing and crystal zone-axis orientation on an adjacent region of the specimen and then moving the specimen to the area of interest for TEM imaging. In addition, the e-beam was on the sample only when taking the images to minimize any e-beam induced oxide reduction.

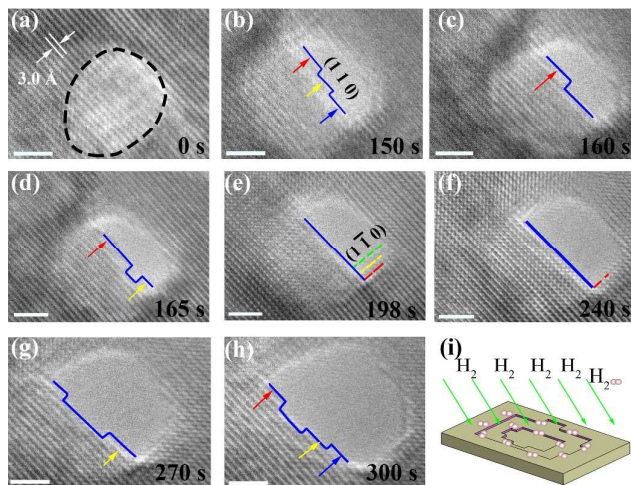


**Fig. 1** (a-h) Time-resolved HRTEM images showing oxide reduction in the local region, resulting in the formation of a nanoscale hole during the reduction of a  $\text{Cu}_2\text{O}(100)$  thin film at  $T = 350^\circ\text{C}$  and  $\text{pH}_2 = 1.2 \times 10^{-2}$  Torr. Scale bar, 2 nm (a-h). (i) Schematic illustrating the inhomogeneous oxide reduction induced by the preferential adsorption of hydrogen at surface defect sites.

Fig. 1 presents in-situ high-resolution TEM images, first in plan view and then in cross section, of the reduction of a  $\text{Cu}_2\text{O}(100)$  film at  $T = 350^\circ\text{C}$  and  $\text{pH}_2 = 1.2 \times 10^{-2}$  Torr. As can be clearly seen, an area with lighter contrast in the image (marked by the black dashed circle in Fig. 1(a)) appears as the reduction proceeds. This suggests that the oxide is reduced in the local area, which results in a thinned region (it is worth noting here that the field of view is under uniform and homogeneous illumination of the e-beam and the oxide would be reduced homogeneously across the area if there is e-beam induced oxide reduction). This trend in the inhomogeneous reduction of the oxide film is further confirmed from in-situ TEM observations that provide atomic detail of the nanoscale hole formation by the local oxide reduction of the oxide film. As shown in Fig. 1(b), the continued oxide reduction in the local area results in a tiny hole with multiple atomic steps along the (110) edge, as indicated by the red, yellow, and blue arrows at different atomic layers. The hole formation also allows for visualizing the oxide reduction process in the cross-sectional view. As shown in Figs. 1(b-h), the oxide reduction involves lateral propagation of (110)-type atomic steps, for which the entire terrace is removed by step flow, resulting in a flattened terrace (Fig. 1(c)). Meanwhile, the nucleation of new (110)-type steps/kinks also occurs at the flattened terrace, which results in a locally one-atomic-layer deeper pit, as indicated by the arrow in Fig. 1(d). The newly formed steps then rapidly propagate laterally, leading to the removal of an additional terrace from the surface (Figs. 1(e-f)). This process of the nucleation and lateral propagation of atomic steps at the free surfaces around the hole results in the gradual enlargement of the hole in the oxide film, as seen in Figs. 1(c-h). While it is not easy to discern the presence of surface defects like atomic steps from the plan-view TEM image shown in Fig. 1(a), the nanoscale hole

formation from oxide reduction in the local area suggests that the oxide surface has a higher concentration of surface defects (atomic steps and kinks) in the local area, which results in the adsorption of more hydrogen at the defective sites that leads to locally faster oxide reduction, as illustrated schematically in Fig. 1(i). This is further confirmed by the in-situ TEM imaging from the cross-sectional view as shown in Figs. 1(b-h), which shows that surface defects play a key role in controlling the oxide reduction process, i.e., the oxide reduction occurs via the retraction of atomic steps at the oxide surface.

The observed oxide reduction process suggests that hydrogen preferentially adsorbs at atomic steps and kink sites, where hydrogen reacts with under-coordinated oxygen atoms to form  $\text{H}_2\text{O}$  molecules that desorb from the surface. The  $\text{H}_2\text{O}$  formation induces the departure of lattice oxygen at the atomic steps. This subsequently makes Cu atoms within the step edge significantly under-coordinated, and these are then prone to detach from the step edge and migrate away. Therefore, the surface steps are observed to undergo retraction, as seen in Figs. 1(b-h).

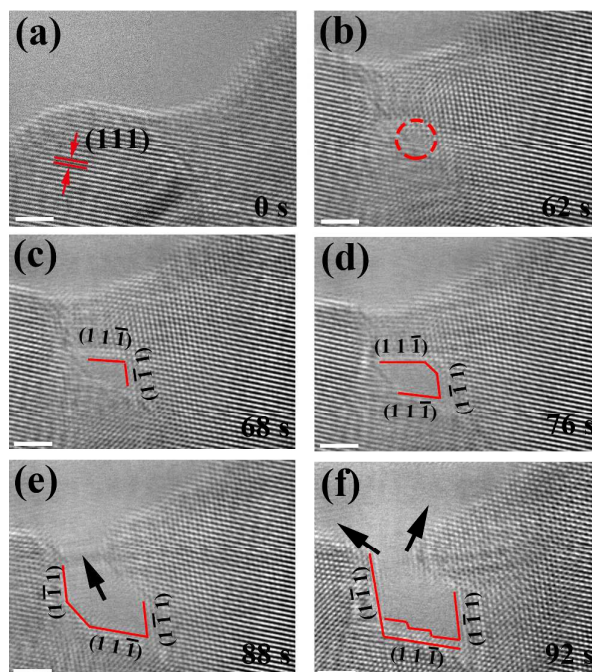


**Fig. 2** Time-resolved HRTEM imaging of the reduction of a  $\text{Cu}_2\text{O}(110)$  thin film at  $T = 350^\circ\text{C}$  and  $\text{pH}_2 = 1.2 \times 10^{-2}$  Torr. The oxide reduction in the local region results in the nucleation and growth of a nano hole in the oxide film. Scale bar, 2 nm.

Such inhomogeneous oxide reduction is also observed from the (110) oriented  $\text{Cu}_2\text{O}$  thin film. Fig. 2 shows a time sequence of HRTEM images illustrating the local reduction of a  $\text{Cu}_2\text{O}(110)$  thin film at  $T = 350^\circ\text{C}$  and  $\text{pH}_2 = 1.2 \times 10^{-2}$  Torr. As seen in Fig. 2(a), the  $\text{Cu}_2\text{O}$  thin film initially has a relatively uniform thickness. As the oxide reduction proceeds, a small hole nucleates and develops locally, as indicated by the red-dashed circle in Fig. 2(b). With continued reduction, the hole grows bigger, {111}-type facets develop along the hole edge and the reduction process can be visualized at the (111) surface via a cross-section view of the (111) facet (Figs. 2(c-f)). As seen in Fig. 2(d), atomic steps form at the (111) surface and their lateral retraction results in the hole enlargement. The surface becomes flattened with the lateral propagation of the

atomic steps to the corner regions (Fig. 2(e)), and new monoatomic steps form at the flattened surface, as outlined by the red lines in Fig. 2(f). These newly formed steps again undergo rapid lateral retraction along the surface. The hole growth through the decay of surface steps gradually leads to the opening of the hole toward the surface side, as indicated by the arrows in Figs. 2(e, f).

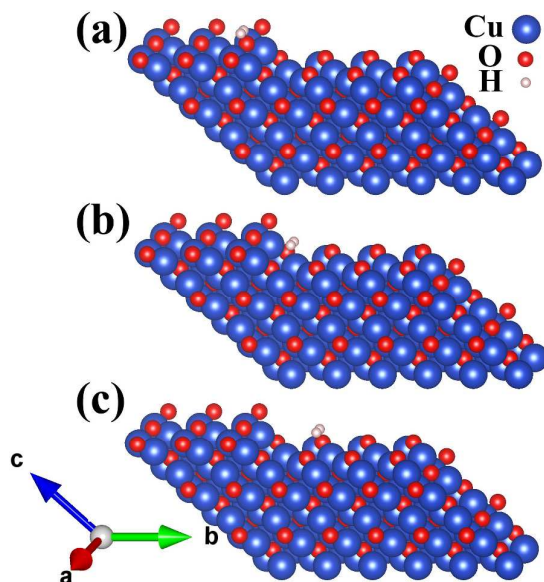


**Fig. 3** Schematic views showing the atomic configuration of the step edge for DFT calculations of hydrogen adsorption at the different sites of the step edge, (a) hydrogen adsorption at the upper step edge, (b) hydrogen adsorption at the (110) microfacet of the step edge, (c) hydrogen adsorption at the bottom of the step edge.

The in-situ TEM observations described above show that the oxide reduction occurs preferentially at surface defect sites on both the  $\text{Cu}_2\text{O}(110)$  and (111) surfaces, suggesting that the phenomenon is not tied to a particular step-edge configuration. The oxide reduction by the flow of surface steps indicates that surface steps are effective trapping centers for hydrogen adsorption, where the trapped hydrogen reacts with under-coordinated O atoms at the step edges, thereby freeing Cu atoms by step-edge detachment. That oxide reduction occurs by surface-step flow is further confirmed using density-functional theory (DFT) modelling of hydrogen adsorption at stepped surfaces (see **Supplementary Note 2** for computational detail). As illustrated in Fig. 3, we construct a stepped surface consisting of a (100) terrace and a half-unit-cell wide (110) micro facet, and then examine the adsorption of  $\text{H}_2$  molecules at different surface sites, including the step edge and the terrace region. Our DFT calculations indicate that the adsorption energies for hydrogen at the upper step edge, the (110) microfacet and the bottom of the step edge are  $-2.34$  eV,  $-1.76$  eV and  $-2.37$  eV, respectively (Fig. 3(a-c)). By contrast, the hydrogen adsorption energy is only  $-1.22$  eV for a terrace site. Therefore, hydrogen adsorbs preferentially along both the upper and lower sides of the step edge and reacts with adjacent O atoms to form  $\text{H}_2\text{O}$  molecules that desorb from the surface and destabilize Cu atoms within the step edge. The freed Cu atoms by step-edge detachment migrate to the Cu substrate via surface diffusion across the oxide surface because Cu adatoms are energetically more favourable to stay on the Cu substrate than on the oxide surface (see **Supplementary Note 2**). Meanwhile, the energy

barriers for the surface diffusion of Cu atoms on  $\text{Cu}_2\text{O}(100)$  are calculated to be  $0.52$  eV and  $0.33$  eV along the [01-1] and [011] directions of the surface, respectively (see **Supplementary Note 2**). The relatively small energy barriers for surface diffusion of Cu atoms released from the step edge also facilitate the oxide reduction induced step-flow motion of the atomic steps.

As shown in our in-situ TEM experiments, the observed oxide reduction is surface specific. This also corroborates well with our previous DFT modelling, which showed that molecular hydrogen adsorption is more favourable than atomic hydrogen adsorption.<sup>23</sup> For molecular hydrogen, surface adsorption should be both kinetically and energetically more favourable than the penetration of molecular hydrogen into the bulk. If there is some dissociative hydrogen adsorption that may result in atomic hydrogen diffusing deep into the bulk, the oxide reduction in the bulk can be still kinetically sluggish because the formed  $\text{H}_2\text{O}$  molecules have to diffuse through the oxide lattice. Therefore, the oxide reduction is dominated at the surface and controlled by surface defects as shown from our in-situ TEM observations.

In summary, we have provided direct evidence for the correlation between the heterogeneous oxide reduction and the retraction of surface steps during the oxide reduction. Using a combination of in-situ atomic-scale TEM imaging and DFT calculations, we show that hydrogen adsorbs preferentially at step edges and induces oxygen loss by reacting with under-coordinated oxygen atoms. The departure of the oxygen atoms also makes Cu atoms within the step edge significantly under-coordinated, which then detach from the step edge and migrate away via surface diffusion. We expect broader applicability of our results in manipulating the oxide reduction process because atomic steps are a common defect to crystal surfaces.

This work was supported by the U.S. Department of Energy, Office of Basic Energy Sciences, Division of Materials Sciences and Engineering under Award No. DE-SC0001135. This research used resources of the Center for Functional Nanomaterials, which is a U.S. DOE Office of Science Facility at Brookhaven National Laboratory under Contract No. DE-SC0012704. This work used the computational resources from the Extreme Science and Engineering Discovery Environment (XSEDE), which is supported by National Science Foundation grant number OCI-1053575.

## Notes and references

- 1 K. C. Potter, C. W. Beckerle, F. C. Jentoft, E. Schwerdtfeger and M. P. McDaniel, *J. Catal.*, 2016, **344**, 657–668.
- 2 A. P. Lagrow, M. R. Ward, D. C. Lloyd, P. L. Gai and E. D. Boyes, *J. Am. Chem. Soc.*, 2017, **139**, 179–185.
- 3 L. Yuan, Q. Yin, Y. Wang and G. Zhou, *Chem. Phys. Lett.*, 2013, **590**, 92–96.
- 4 J. a. Rodriguez, J. C. Hanson, A. I. Frenkel, J. Y. Kim and M. Pérez, *J. Am. Chem. Soc.*, 2002, **124**, 346–354.
- 5 H.-C. Jeong and E. D. Williams, *Surf. Sci. Rep.*, 1999, **34**, 171–294.
- 6 W. D. Bond, *J. Phys. Chem.*, 1962, **66**, 1573–1577.
- 7 F. Yang, Y. Choi, P. Liu, J. Hrbek and J. a. Rodriguez, *J. Phys. Chem. C*, 2010, 17042–17050.
- 8 J. Pike, S. W. Chan, F. Zhang, X. Wang and J. Hanson, *Appl.*

## COMMUNICATION

ChemComm

- Catal. A Gen.*, 2006, **303**, 273–277.
- 9 H. Qin, X. Chen, J. Li, P. Sutter and G. Zhou, *J. Phys. Chem. C*, 2017, **121**, 22846–22853.
- 10 K. Schulz and D. Cox, *Surf. Sci.*, 1992, **278**, 10027.
- 11 L. M. Molina and B. Hammer, *Phys. Rev. B - Condens. Matter Mater. Phys.*, 2004, **69**, 1–22.
- 12 L. Martin, G. Vallverdu, H. Martinez, F. Le Cras and I. Baraille, *J. Mater. Chem.*, 2012, **22**, 22063.
- 13 P. L. Hansen, J. B. Wagner, S. Helveg, J. R. Rostrup-Nielsen, B. S. Clausen and H. Topsøe, *Science*, 2002, **295**, 2053–2055.
- 14 J. A. Rodriguez, J. C. Hanson, A. I. Frenkel, J. Y. Kim and M. Pérez, *J. Am. Chem. Soc.*, 2002, **124**, 346–354.
- 15 X. Wang, J. C. Hanson, A. I. Frenkel, J. Y. Kim and J. A. Rodriguez, *J. Phys. Chem. B*, 2004, **108**, 13667–13673.
- 16 T. Fujita, P. Guan, K. McKenna, X. Lang, A. Hirata, L. Zhang, T. Tokunaga, S. Arai, Y. Yamamoto, N. Tanaka, Y. Ishikawa, N. Asao, Y. Yamamoto, J. Erlebacher and M. Chen, *Nat. Mater.*, 2012, **11**, 775–780.
- 17 L. Zou, J. Li, D. Zakharov, E. A. Stach and G. Zhou, *Nat. Commun.*, 2017, **8**, 307.
- 18 Y. A. Wu, L. Li, Z. Li, A. Kinaci, M. K. Y. Chan, Y. Sun, J. R. Guest, I. McNulty, T. Rajh and Y. Liu, *ACS Nano*, 2016, **10**, 3738–3746.
- 19 R. Sharma, *Microsc. Microanal.*, 2001, **7**, 494–506.
- 20 D. B. Williams and Carter Barry, *Transmission Electron Microscopy*, 2009.
- 21 W. Zhu, J. P. Winterstein, W. C. D. Yang, L. Yuan, R. Sharma and G. Zhou, *ACS Nano*, 2017, **11**, 656–664.
- 22 A. P. Lagrow, M. R. Ward, D. C. Lloyd, P. L. Gai and E. D. Boyes, *J. Am. Chem. Soc.*, 2017, **139**, 179–185.
- 23 W. Shan, Q. Liu, J. Li, N. Cai, W. A. Saidi and G. Zhou, *J. Chem. Phys.*, , DOI:10.1063/1.4972070.